Optical control of spin textures in quasi-one-dimensional polariton condensates

C. Antón,[1,2] S. Morina,[3] T. Gao,[4,5] P. S. Eldridge,[4] T. C. H. Liew,[3] M. D. Martín,[1,2] Z. Hatzopoulos,[4,6] P. G. Savvidis,[4,5] I. A. Shelykh,[3] and L. Viña[1,2,7,*]

[1]*Departamento de Física de Materiales, Universidad Autónoma de Madrid, Madrid 28049, Spain*
[2]*Instituto de Ciencia de Materiales "Nicolás Cabrera," Universidad Autónoma de Madrid, Madrid 28049, Spain*
[3]*School of Physical and Mathematical Sciences, Nanyang Technological University, 637371, Singapore*
[4]*FORTH-IESL, P.O. Box 1385, 71110 Heraklion, Crete, Greece*
[5]*Department of Materials Science and Technology, University of Crete, 71003 Heraklion, Crete, Greece*
[6]*Department of Physics, University of Crete, 71003 Heraklion, Crete, Greece*
[7]*Instituto de Física de la Materia Condensada, Universidad Autónoma de Madrid, Madrid 28049, Spain*

(Received 30 October 2014; revised manuscript received 27 January 2015; published 10 February 2015)

We investigate spin transport through polarization-resolved spectroscopy by propagating polariton condensates in a quasi-one-dimensional microcavity ridge along macroscopic distances. Under circularly polarized, continuous-wave, nonresonant excitation, a sinusoidal precession of the spin in real space is observed whose phase depends on the emission energy. The experiments are compared with simulations of the spinor-polariton condensate dynamics based on a generalized Gross-Pitaevskii equation, modified to account for incoherent pumping, decay, and energy relaxation within the condensate.

DOI: 10.1103/PhysRevB.91.075305 PACS number(s): 67.10.Jn, 78.67.De, 71.36.+c, 72.25.Dc

I. INTRODUCTION

Semiconductor microcavities (MCs) in the strong-coupling regime are excellent candidates for designing novel "spinoptronic" devices due to their strong optical nonlinearities [1], polarization properties [2–4], and fast spin dynamics [5]. The control of polariton condensate propagation and their polarization [4] provide the necessary ingredients for future optical circuits. The first steps toward the fabrication of spin-based polariton condensate switches [6–9], gates [10], and memories [11,12] have been recently achieved. They fulfill the fundamental technological requirements for the operation with polarization-encoded signals: micrometric size, nonlocal action triggering and high speeds (of the order of $\sim$1 μm/ps due to the ballistic polariton propagation). New schemes for the realization of spinoptronics devices [13,14] and "polariton neurons" in circuits, the building blocks of all-optical integrated logic circuits [15–17], have been recently proposed. One-dimensional (1D) and quasi-1D patterned high-finesse MCs provide an ideal platform for all-optical manipulation [18], ballistic propagation and amplification [19], and gating of polariton condensates [20–25]. The waveguide nature of these structures induces the channeling of polariton propagation, while the discretization of energy levels results in a rich relaxation dynamics [26,27].

In planar semiconductor MCs, the splitting of the transverse electric (TE) and magnetic (TM) modes of the cavity [28] induces an effective magnetic field, which on its own produces a precession of the polaritons spin, when they propagate over macroscopic distances. This effect is well known as the optical spin Hall effect [4,29], and it was first predicted by Kavokin and co-workers [30] as an analog of the electronic spin Hall effect [31,32]. Initial experiments were conducted with resonant excitation [29] making use of Rayleigh scattering [33] or tightly focused laser spots [34] to excite multiple states in reciprocal space. These experiments represented purely linear effects, not relying on the excitonic component of polaritons [35]. The presence of quantum-well excitons is required for nonresonant excitation, leading to the spontaneous formation of a propagating polariton condensate [4]. The effective magnetic field representing the optical spin Hall effect can be utilized, for example, to generate polarization textures [4,36], where the polaritons propagate in rings spreading in real space, showing oscillations of the polarization degree in azimuthal angle and time; to convert the spin to orbital angular momentum [37]; to create spin-polarized vortices [37–40]; and to form half-dark solitons [41,42] and very similar structures [43] in the wake of an obstacle. Recent theoretical work has also examined the role of the optical spin Hall effect in driving polarized bright solitons [44] and other spin patterns [45,46].

In this work, we investigate optically the collective spin dynamics of polariton condensates moving along macroscopic distances in a quasi-1D MC ridge. The discretization in energy of the lower polariton branch (LPB) in our quasiconfined structure has notable consequences in the coherent transport of the spin vector. In the first place, the confinement renders a TE-TM mode splitting, which remains for zero in-plane wave vector, and it acquires larger values than the TE-TM splitting in two-dimensional (2D) MCs. Furthermore, a spectral analysis of the spin transport reveals different polariton spin textures from those observed in 2D systems [4]. The richness of these textures is related to the energy-dependent speed of propagation of polaritons in our system with lowered dimensionality. The ballistic propagation of spin-polarized polaritons along the ridge is observed over distances of $\sim$100 μm.

To describe the polarization state of exciton-polaritons, we adopt the pseudospin formalism [47]. Polaritons possess a spin with two possible projections on the structural growth axis of the MC. The polarization of the emitted light gives direct access to the pseudospin state, which is fully characterized by the four-component Stokes vector $\vec{s} = (s_0, s_x, s_y, s_z)$. Here, s_0 is the total photoluminescence (PL) intensity, and

*luis.vina@uam.es

$s_{x,y,z} = (I_{H,D,\sigma^+} - I_{V,A,\sigma^-})/(I_{H,D,\sigma^+} + I_{V,A,\sigma^-})$. I_{H,D,σ^+} and I_{V,A,σ^-} are the measured intensities in the horizontal (H) and vertical (V), the diagonal (D) and antidiagonal (A), and the two circular polarization components σ^+ and σ^-.

This paper is organized as follows. In Sec. II we discuss the sample and the experimental setup. In Sec. III we present and discuss our results; we first show, under continuous wave (cw) excitation, the optical spin Hall effect [4,30] in a quasi-1D structure, discussing the s_z oscillations in real space, for a σ^+-polarized pump. In Sec. III A we systematically investigate the distribution of the Stokes components as a function of the PL energy and position along the ridge. In Sec. III B we demonstrate that the s_z precession is lost under linear excitation and/or high-power excitation conditions. In Sec. IV the experiments are compared with simulations of the spinor-polariton condensate dynamics based on a generalized Gross-Pitaevskii equation, modified to account for incoherent pumping, decay, and energy relaxation within the condensate. Finally, in Sec. V we provide the conclusions of this work.

II. SAMPLE AND EXPERIMENTAL SETUP

A high-quality $5\lambda/2$ AlGaAs-based MC with 12 embedded quantum wells is investigated, whose Rabi splitting, Ω_R, amounts to 9 meV. Ridges, with dimensions 20×300 μm^2, have been obtained by reactive ion etching (further information about this sample is given in Ref. [48]). We study a ridge situated in a region of the sample corresponding to resonance (detuning between bare exciton and cavity modes is $\backsim 0$). The sample is kept at 10 K in a cold-finger cryostat and it is excited with a cw laser, tuned to the first high-energy Bragg mode of the MC (1.612 eV). The cw laser is chopped at 300 Hz with an on/off ratio of 1:2 in order to prevent unwanted sample heating. We focus the laser beam on the sample through a microscope objective to form a 10 μm $-$ $\varnothing$ spot. The same objective is used to collect (angular range $\pm 18^\circ$) the PL, which is directed toward a 0.5 m imaging spectrometer. The power threshold for polariton condensation is $P_{\rm th} = 2$ mW.

In our experiments, polaritons propagate predominantly along the x axis of the ridge [see Fig. 1(a)]. Therefore, in all the images presented in the paper, where the y direction is not shown, the spectral PL distribution is analyzed along the x axis from a $\Delta y = 2$-μm-wide central region of the ridge. However, for the sake of completeness, the full 2D polariton intensity and degree of circular polarization distributions are presented when appropriate.

We start by describing the dispersion relations of polaritons along two orthogonal directions in the ridge, k_x at $k_y = 0$ and k_y at $k_x = 0$. The confinement in the y axis of the ridge results in the discretization of the k_y in-plane momentum, splitting the LPB in many subbands, Fig. 1(b), whose antinodes along k_y are visible in Fig. 1(d). It is important to emphasize that only even subbands are visible in Fig. 1(b), since along k_x we spectrally resolve the PL at $k_y = 0$. Odd modes (with a node at $\mathbf{k} = \mathbf{0}$) are visible in Fig. 1(d); see, for example, the subband at 1.5405 eV. The scenario seen in these dispersion relations is very interesting because it reveals the possibility of parametric scattering processes among many different subbranches. Recent works on 1D semiconductor MCs exploit these extra-confinement effects to study new

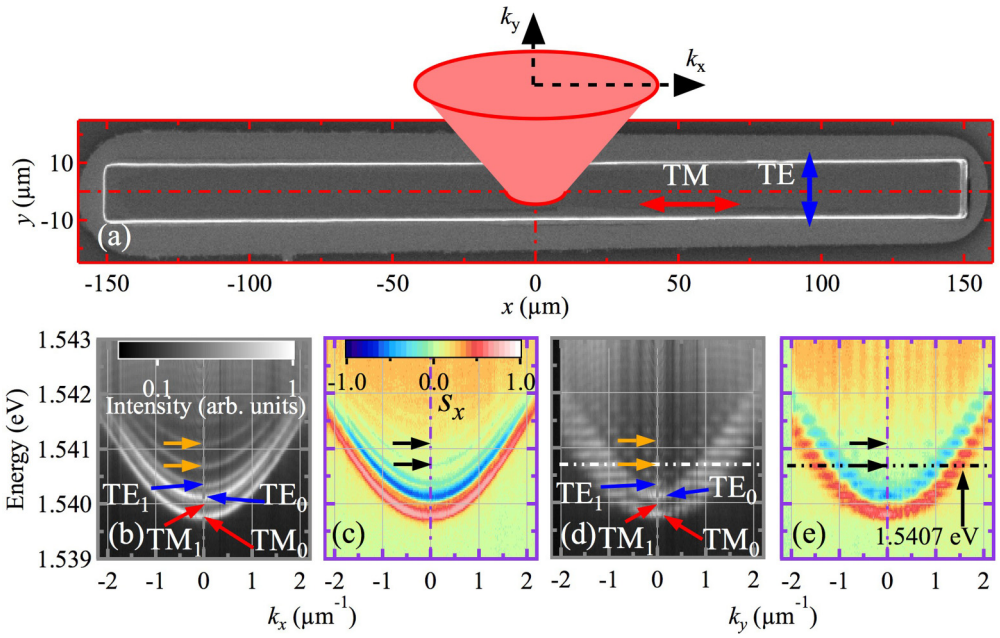

FIG. 1. (Color online) (a) Scanning electron microscopy image of a 20-μm-wide ridge, including an angular scheme of the PL emitted from the center of the ridge (see the cone of light as a guide to the eye); the z direction is perpendicular to the plane of the paper. The bottom panels display, under nonresonant (1.612 eV), weak, circularly polarized light excitation: (b) and (d) energy dispersions of the PL along k_x and k_y, respectively; (c) and (e) linear degree of polarization (s_x) vs energy and k_x and k_y, respectively. Dot-dot-dashed white and black lines in panels (d,e) mark the energy value (1.5407 eV) used for Fig. 2(b). Red and blue arrows in panels (a,b,d) mark the TM and TE character of the even subbands in the dispersion relations, respectively. Orange and black arrows in panels (b)–(e) mark the energy positions of weakly polarized, consecutive higher subbands. The PL and s_x are coded in linear, normalized, false color scales.

parametric phenomena (see, for example, Refs. [49,50] and references therein).

Confinement in a quasi-1D cavity enhances the splitting between the two light polarizations TM and TE, parallel and perpendicular to the x axis of the ridge, respectively. We identify TM (TE) as the H (V) direction used to define the linear degree of polarization (s_x). Considering the k_x direction, the lowest energy subband is TM_0-polarized, see the label in Fig. 1(b), and its corresponding s_x is shown in Fig. 1(c), where an intense, red subband appears, whose minimum is at $E = 1.5397$ eV and $k_x = 0$. The next TM_1 mode is 0.2 meV blueshifted, lying very close to the TE_0 mode [intense blue subband in Fig. 1(c)]. The splitting between TM_0 and TE_0 is 0.36 meV. Higher energy modes, with a weaker degree of polarization, are visible at 1.5407 and 1.5411 eV, marked by orange and black arrows in Figs. 1(b) and 1(d) and Figs. 1(c) and 1(e), respectively. Analyzing the dispersion relation k_y, Figs. 1(d) and 1(e), a further, horizontal discretization of the energy levels is clearly observed. The separation in k_y between consecutive antinodes of a single state is $\sim 0.4\ \mu m^{-1}$.

Detailed spectra at $k_x = 0$, both for intensity (thick, gray line) and s_x (thin, purple line), are given in Fig. 2(a), with different, labeled modes indicated by arrows. The aforementioned higher-energy modes are marked by orange arrows. Figure 2(b) details a profile of the PL and s_x versus k_y, at $E = 1.5407$ eV: the predominant structures at $|0.7| < k_y < |1.8|\ \mu m^{-1}$ shown by the thick gray line are constituted by

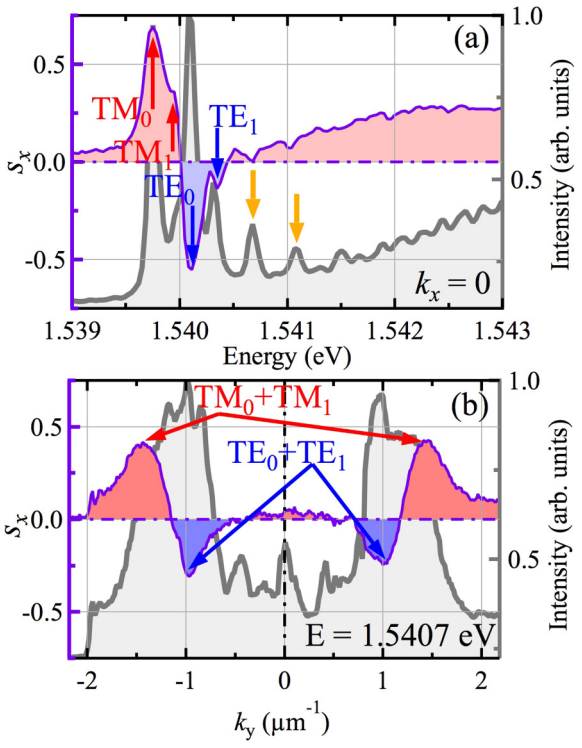

FIG. 2. (Color online) (a) PL (s_x) as a function of energy at $k_x = 0$ in a gray, thick (purple, thin) line. (b) PL (s_x) as a function of k_y at $E = 1.5407$ eV in a gray, thick (purple, thin) line. Red and blue arrows in panels (a) and (b) mark the TM and TE character of the even subbands in the dispersion relations, respectively. Orange arrows in panel (a) mark the energy positions of weakly polarized, higher subbands.

the modes ($TM_0 + TM_1$) and ($TE_0 + TE_1$) at high k_y values, while the three central antinodes correspond to other confined modes at lower k_y values. Only when a polarization analysis is performed are TE and TM distributions resolved (thin purple line), as marked in the figure.

Assuming a square-well-type potential in the y direction, the energies of the TM- and TE-polarized photonic modes can be approximated by

$$E_{C;\mathrm{TM,TE}}(n,k_x) = \frac{(n+1)^2\hbar^2\pi^2}{2m_C L_y^2} + \frac{\hbar^2 k_x^2}{2m_C} \pm \Delta_{\mathrm{TM,TE}}, \quad (1)$$

where $n = 0,1,2,\ldots$ is the subband index, m_C is the photon effective mass, L_y is the ridge width, and $\Delta_{\mathrm{TM,TE}}$ characterizes the splitting between the H and V polarizations. The dispersion of the upper (+) and lower (−) polariton modes is given by the standard two-oscillator formula (up to a constant energy shift):

$$E^{\pm}_{\mathrm{TM,TE}}(n,k_x) = \tfrac{1}{2}E_{C;\mathrm{TM,TE}}(n,k_x) \pm \sqrt{E^2_{C;\mathrm{TM,TE}}(n,k_x) + 4\Omega^2}, \quad (2)$$

where $\Omega = \Omega_R/2$ is the exciton-photon coupling constant. Assuming a Lorentzian line shape (corresponding to 18 ps lifetime) and an independent Boltzmann population of the TM- and TE-polarized energy levels ($T = 10$ K), we calculate the dispersions corresponding to lower polariton modes (E^-) shown in Fig. 3. As in the experiments, we show the $k_y = 0$ ($k_x = 0$) PL when resolving the dispersion along k_x (k_y). The results show that the TM bands are hidden by the stronger populated TE bands at higher energies.

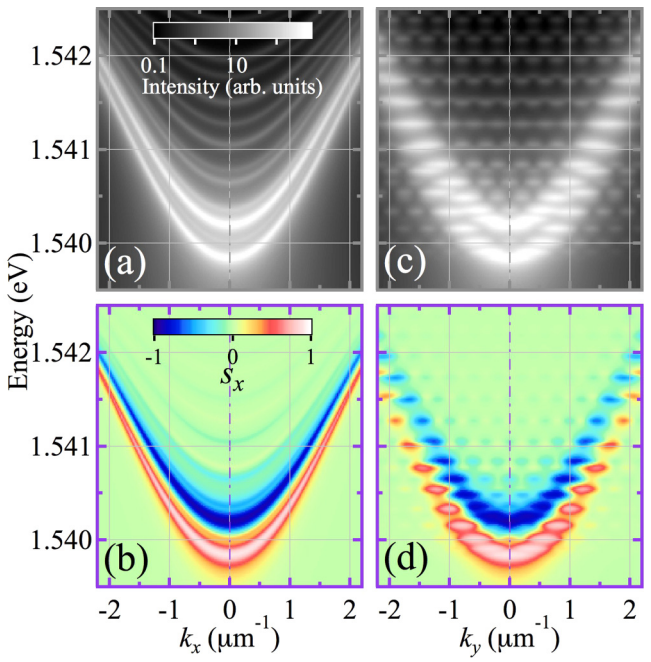

FIG. 3. (Color online) (a) and (c) Theoretical energy dispersion relation of lower polariton modes along k_x (at $k_y = 0$) and k_y (at $k_x = 0$), respectively; (b) and (d) corresponding linear degree of polarization (s_x). The intensity and s_x are coded in linear, normalized, false color scales.

III. EXPERIMENTAL RESULTS AND DISCUSSION

Recently, Kammann and co-workers reported an analog of the optical spin Hall effect of an exciton-polariton condensate in a planar MC, under cw, nonresonant, circularly polarized excitation [4]. Circularly polarized condensates propagate over macroscopic distances, while the collective condensate spins coherently precess around an effective magnetic field. This effective magnetic field can be expressed as $\vec{H}_{\text{eff}} = \frac{\hbar}{\mu_B g}\vec{\Omega}_k$, where μ_B is the Bohr magneton, g is the electron g factor, and $\vec{\Omega}_k$ is the in-plane vector with the following components:

$$\Omega_x = \frac{\Delta_{\text{TM,TE}}}{\hbar k^2}\left(k_x^2 - k_y^2\right), \quad \Omega_y = \frac{\Delta_{\text{TM,TE}}}{\hbar k^2}k_x k_y, \qquad (3)$$

where $\vec{k} = (k_x, k_y)$ is the in-plane wave vector of the polariton.

Here we study a similar phenomenon in our quasi-1D structure: we start by focusing on the polariton distribution in real space and its degree of circular polarization, under cw, circular excitation, without resolving the PL energy.

Figure 4(a) shows the energy-integrated distribution of the polariton PL in real space, under σ^+-polarized, nonresonant excitation at $(x, y) = (0,0)$ with a pump power of $3.75 \times P_{\text{th}}$. The pump creates outflowing polariton condensates due to the repulsive interactions with the excitonic reservoir [18,27]. The propagation inside the ridge is not purely 1D since slanted traces of the polariton flow are visible (see the white dashed arrows as a guide to the eyes), as a result of the reflection of the fluid against the lateral borders at $y = \pm 10$ μm. Interference patterns in the PL, due to polariton-polariton scattering, are also observed (see, for example, the region enclosed by a dashed box). This effect has also been reported in the 2D case [51]. A fast Fourier transform (FFT) of this enclosed region, shown in Fig. 4(c), obtains the frequencies corresponding to counterpropagating polariton wave packets, with a difference in momentum propagation of $\Delta K_x \approx 3.4$ μm^{-1} (see the area enclosed by a dot-dashed box). The corresponding value of k_x matches the typical speed of polariton wave packets in 1D systems ($\sim$1 μm/ps) [19,27].

Outside the pump spot, the potential energy is converted into kinetic energy. Polaritons also relax and lose energy through scattering with the excitonic reservoir and through intra-branch scattering [23,26,27]; the energy of condensed polaritons spans $\sim$1.5 meV across the subbands (see below). Therefore, the description of the spin distribution in our quasi-1D structure, in the presence of polariton energy relaxation, becomes more complex than in two dimensions (where the ballistic spin precession occurs in a simpler dispersion relation). However, for the sake of simplicity, we show in Fig. 4(b) the energy-integrated distribution of the circularly polarized component of the PL (s_z). The large red area in the central region corresponds to the predominantly spin-up aligned polaritons at the excitation area. The spin of leftward and rightward propagating polaritons precesses with a periodicity of $\sim$40 μm (see the up- and down-arrows). The energy integration is responsible for the relatively low values of s_z. In Fig. 4(d), we quantify both the total PL (thick gray line) and s_z (thin purple line) as a function of x at the central cross section of the ridge ($y = 0$). The oscillations in the PL are caused by the fluid reflections against the borders of the

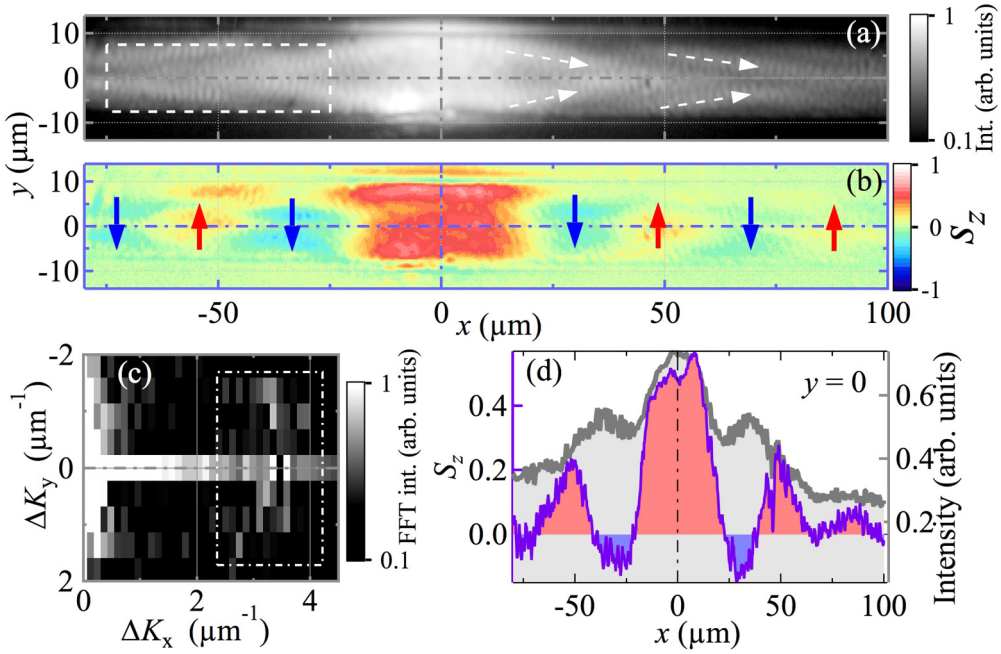

FIG. 4. (Color online) Collective polariton condensate spin precession in a quasi-1D ridge. (a) Polariton PL distribution in real space under nonresonant (1.612 eV), circularly polarized (σ^+) excitation at the center of the ridge. The pump power is $3.75 \times P_{\text{th}}$. Dashed white arrows sketch the direction of the polariton flow along its propagation. (b) Corresponding circular degree of polarization distribution (s_z). Vertical blue and red arrows highlight the spin precession, oscillating from negative (σ^-) to positive (σ^+) values, respectively. (c) FFT intensity of the region enclosed by a dashed, white rectangle in panel (a). The dot-dashed, white rectangle marks the region of relevant frequencies arising from interferences between propagating and backscattered polaritons in real space. The PL and the FFT map are coded in a logarithmic, false color scale, while a linear one is used for s_z. (d) PL (s_z) vs x in the central region of the ridge $y = 0$, plotted with a thick gray (thin purple) line.

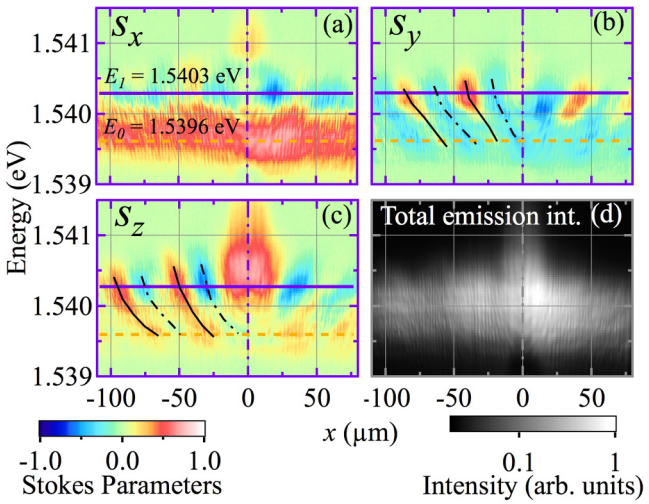

FIG. 5. (Color online) Stokes parameters of the polariton PL as a function of energy and spatial position (x): (a) s_x, (b) s_y, and (c) s_z, respectively, under nonresonant (1.612 eV), circularly polarized (σ^+) excitation. (d) Corresponding PL. The pump power is $3.75 \times P_{\text{th}}$. Slanted, dot-dashed (solid) lines in panels (b) and (c) sketch the continuous shift with energy of the minima (maxima) values of s_y and s_z. The horizontal purple, solid (orange, dashed) line at $E_1 = 1.5403$ eV ($E_0 = 1.5396$ eV) marks the energy of interest used for the data depicted in Fig. 6. The PL (degree of polarization) is coded in a logarithmic (linear), false color scale.

ridge, obtaining large intensities when polaritons merge at the center [see the arrows in Fig. 4(a)]. The spin oscillation and its damping along its propagation are clearly visible (thin purple line). Note that the periodicities of the PL and the spin oscillations do not match since they arise from different phenomena.

A. PL spectroscopy on the spin Hall effect

Figure 5 shows the energy- and space-resolved Stokes components of the polarized PL under the same excitation conditions as those described in Fig. 4. The polariton condensates span an energy of 1.5 meV around ∼1.540 eV. We present here a spatial analysis of s_x, s_y, and s_z at two different energies $E_0 = 1.5396$ eV and $E_1 = 1.5403$ eV, which correspond to those of polaritons condensing into the TM's and the TE's subbands [see the dashed and solid horizontal lines in Figs. 5(a)–5(c)], respectively. Figure 5(a) shows a weak spatial oscillation of s_x at E_1. Additionally, a small positive s_x from higher-energy excitons (from 1.5405 to 1.5415 eV) is present at $x = 0$; this was already present in Fig. 1(c), under below-threshold excitation. At E_0, s_x is large and positive, as expected from the TM character of the lowest polariton subband [see Figs. 1(c) and 2(a)]. The diagonal component s_y displays a significant spatial oscillation with a period of ∼40 μm at E_1 [see Fig. 5(b)]. In contrast, s_y barely oscillates around a value of ~ -0.2 at E_0. Figure 5(c) shows a highly σ^+-polarized population at $x = 0$ at E_1 and above, set by the excitation laser. At E_1 the condensed, spreading polaritons exhibit a precessing s_z, again with the same period of ∼40 μm. This precession, although weaker, is also seen at E_0.

These oscillations in the Stokes parameters are similar to those previously reported in planar MCs, considering that in our case the propagation takes place along the ridge channel (equivalent to a given radial direction of the 2D rings; see Fig. 3 of Ref. [4]). The effective magnetic field, induced by the splitting of the TE-TM modes, is responsible for this precession of the polariton spins, while they propagate over the ridge, due to the optical spin Hall effect [30]. The main difference in our case lies in the energy dependence of the precession pattern, giving rise to distinct spin textures. The phase of the spatial s_z oscillations shifts continuously with increasing energies, so that at E_0 and E_1 they are shifted with respect to each other by a π phase approximately. In Figs. 5(b) and 5(c), the slanted, dot-dashed (solid) lines highlight the minimal (maximal) points of the s_y and s_z oscillations across the PL energy, respectively. This phase shift arises from the different propagation speeds of polaritons at different energies: polaritons at higher energies move at higher speeds and therefore travel longer distances for each precession of the spin. Nevertheless, the spin spatial periodicity does not change significantly with energy. Finally, Fig. 5(d) displays, for completeness, the PL along the x axis, from 1.5395 to 1.5405 eV.

In Fig. 6 we detail the different $s_{x,y,z}$ profiles at the two selected energies E_0 and E_1. The dashed line at E_0 shows a constant $s_x \approx 0.5$ profile as a function of x; at E_1 (solid line), s_x varies weakly [see Fig. 6(a)]. Figures 6(b) and 6(c) detail the s_y and s_z oscillations, respectively, at E_0 and E_1. The displacement in real space of the minimal (maximal) points of the s_y and s_z oscillations from the lower energy E_0 to the higher one E_1 is evidenced by straight, dot-dashed (solid) lines.

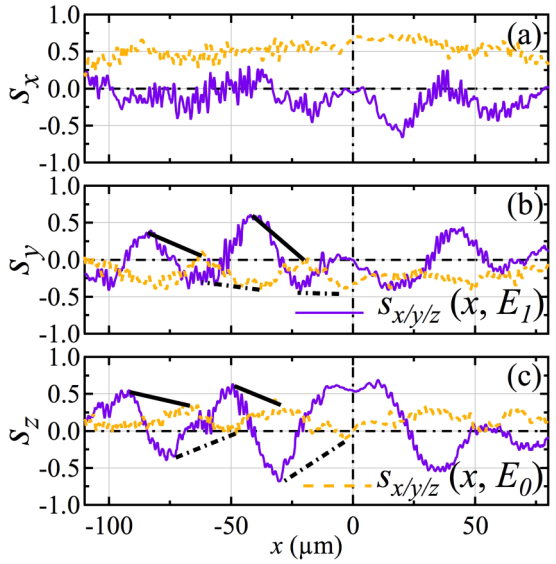

FIG. 6. (Color online) Stokes parameters $s_{x,y,z}$ of the polariton PL as a function of x at energies $E_0 = 1.5396$ eV (dashed line) and $E_1 = 1.5403$ eV (solid line) in panels (a-c), respectively, extracted from Fig. 5. Dot-dashed (solid) lines in panels (b) and (c) are guides to the eye linking the minimum (maximum) value of s_y and s_z at the two energies, respectively, highlighting the spatial shift with energy of their oscillations.

B. Spin-precession collapse

A recent study shows that a transfer of the polarization of a nonresonant excitation laser to polariton condensates occurs for excitation powers slightly above the condensation threshold and that the transfer efficiency decays with increasing pump power [52]. We also profit from the former fact to nonresonantly create polariton condensates with a predominant circular polarization. In this section, we investigate not only the latter fact, i.e., the influence of the pump power, but also that of its spin polarization (circular or linear) on the collective polariton spin state and on its propagation.

Two different pump powers are used for the experiments compiled in Fig. 7: 3.75 (4.75) $\times P_{\rm th}$ for the left (right) column. s_z maps as a function of energy and x under σ^+ (linear excitation) are shown in Figs. 7(a-1) and 7(a-2) [Figs. 7(b-1) and 7(b-2)]. Finally, for the sake of completeness, Figs. 7(c-1) and 7(c-2) show the polariton PL. In Fig. 7(a-1), s_z oscillations are clearly observed from 1.5395 to 1.5408 eV. The σ^+-polarized, nonresonant excitation induces a highly σ^+-polarized, blueshifted population at $x = 0$, whose PL spans from 1.5400 to 1.5415 eV. A 25% increase of the pump power strongly reduces the amplitude of the spin precession, which becomes barely visible in Fig. 7(a-2). These oscillations are also suppressed for linear excitation, as shown in Figs. 7(b-1) and 7(b-2). The PL map at high excitation power, 4.75 $\times P_{\rm th}$, reveals a nonemitting region around $x = 0$ with an energy width of 0.7 meV and a spatial extent full width at half-maximum (FWHM) of $\sim$20 μm, highlighted with a dashed line in Fig. 7(c-2). This dark region is caused by the excitonic reservoir, which ejects polaritons outward from $x = 0$.

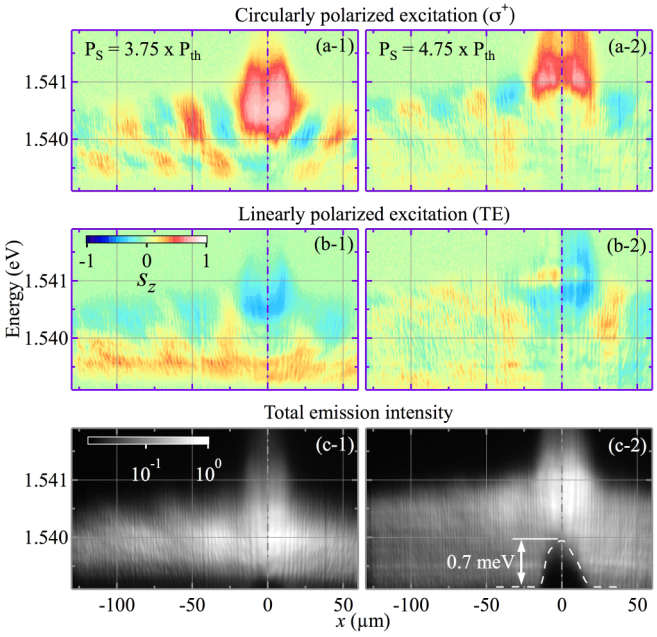

FIG. 7. (Color online) Polariton spin precession and PL as a function of pump power at 3.75 $\times P_{\rm th}$ (left column) and 4.75 $\times P_{\rm th}$ (right column). The nonresonant excitation (1.612 eV) at $x = 0$ is circularly (linearly) polarized in the first (second) row. Panels (a) and (b) depict the circular degree of polarization (s_z); panels (c) show the polariton PL. In panel (c-2) the local repulsive potential induced by photogenerated excitons at $x = 0$ is sketched by a dashed line. The PL (s_z) is coded in a logarithmic (linear) false color scale.

IV. MODEL

To model the spatial structure of polariton condensates, we use a mean-field description including incoherent pumping and decay [53] as well as energy relaxation [26]. This model was used previously to describe the dynamics of condensate transistors in microwire ridges [21,25]. In the current experiment, it is important to use a 2D model that accounts for the subband structure reported in Fig. 1 as well as a two-component spinor wave function to account for the spin degree of freedom. The spinor polariton wave function $\psi_\sigma(\vec{r},t)$ obeys the dynamical equation

$$\begin{aligned} i\hbar\frac{d\psi_\sigma(\vec{r},t)}{dt} = \Big[& \hat{E}_{\rm LP} + (\alpha_1 - i\Gamma_{\rm NL})\,|\psi_\sigma(\vec{r},t)|^2 \\ & + \alpha_2|\psi_{-\sigma}(\vec{r},t)|^2 + V_0(\vec{r}) + V_\sigma(\vec{r}) \\ & + i\left(W_\sigma(\vec{r}) - \frac{\Gamma}{2}\right)\Big]\psi_\sigma(\vec{r},t) \\ & + \Delta_{\rm TM,TE}\psi_{-\sigma} + i\hbar\,\Re[\psi(\vec{r},t)], \end{aligned} \tag{4}$$

where $\sigma = \pm$ denotes the two circular polarizations of polaritons. α_1 and α_2 represent the strengths of interactions between polaritons with parallel and antiparallel spins, respectively. The operator $\hat{E}_{\rm LP} = -\frac{\hbar^2\hat{\nabla}^2}{2m_P}$ represents the parabolic dispersion of the LPB [read LP in Eq. (4)]. Here, $\vec{r}$ is a two-component vector consisting of the real-space coordinates lying on the ridge, the origin of this coordinate system being in the center of the ridge.

Polaritons enter the condensate at a rate determined by $W_\sigma(\vec{r})$, which is both polarization- and space-dependent. While the nonresonant laser used in the experiment is polarized, due to the presence of spin relaxation, one does not expect a full polarization of the photocreated hot excitons. Consequently, we expect a partially polarized reservoir of excitons to drive the polariton condensates, eventually yielding both possible circular polarizations. The condensation rate for the σ^+-polarized polaritons from the excitonic reservoir is given by

$$W_+(\vec{r}) = W_0 e^{-r^2/L^2}, \tag{5}$$

where W_0 is the peak condensation rate and L is the width. In principle, the spatial profile of the condensation rate includes the effects of exciton dispersion, diffraction, and nonlinear repulsion after excitons are excited by the nonresonant laser pump. In practice, the effective mass of excitons is four orders of magnitude larger than that of polaritons, and there is very little spreading of the excitons over length scales relevant for polaritons, such that L can be taken to be the same as the laser pump-spot diameter. The condensation rate for the σ^--polarized polaritons is smaller and given by $W_- = \rho W_+$, where ρ is a parameter that is fitted to the experimental results. In this form, the condensation rate is explicitly spin anisotropic.

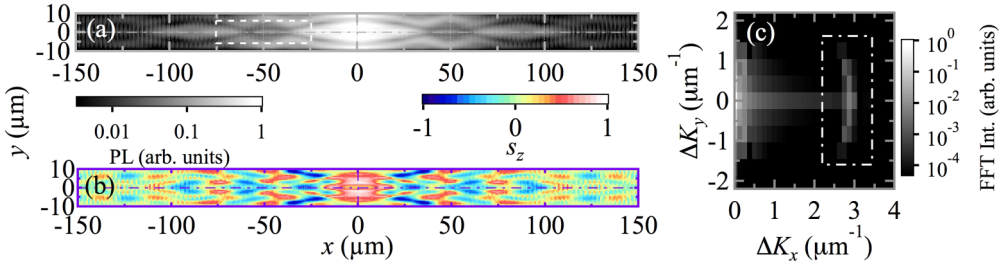

FIG. 8. (Color online) Simulations of the collective polariton condensate spin precession in a quasi-1D ridge. (a) PL rendering polariton distribution in real space under nonresonant, circularly polarized excitation at the center of the ridge, with a pump power $P = 3.75 \times P_{\rm th}$. The dashed, white box marks the spatial region that is Fourier-transformed. (b) Corresponding simulation on the circular degree of polarization distribution (s_z). (c) FFT intensity of the simulated polariton PL distribution in the framed area in panel (a); remarkable Fourier frequencies arise at $\sim 3\ \mu\text{m}^{-1}$ from the counterpropagating polariton populations; see the region delimited by a dot-dashed, white box. The PL and the FFT map are coded in a logarithmic, false color scale, while a linear one is used for s_z.

The spin-dependent effective potential experienced by polaritons can be described by

$$V_\sigma(\vec{r}) = G_\sigma W_\sigma(\vec{r}), \tag{6}$$

where G_σ is a constant representing the strength of forward-scattering processes between excitons in the reservoir and in the condensate.

We also consider a spin-independent component in the effective potential, V_0, which is the profile potential of the ridge. We assume it to be that of a 2D infinite square well, where the confinement in the y direction gives rise to the subband structure observed experimentally (Fig. 1) and theoretically (Fig. 3).

The polaritons decay with a decay rate Γ. They also experience a nonlinear loss corresponding to scattering out of the condensate. According to estimates in Ref. [54], $\Gamma_{\rm NL} \approx 0.3\alpha_1$. Once injected, different circular polarizations are also coupled by the linear polarization splitting Δ_{XY} in the system, which can give rise to oscillations between spin components. While in 2D MCs the dominant polarization splitting is wave-vector-dependent, the dominant splitting in polariton channels is due to strain giving an anisotropic lattice constant [55]. A splitting occurs between polarizations aligned parallel and perpendicular to the channel axis, which remains for the zero in-plane wave vector [as can be seen in Figs. 1(c) and 1(e)], and takes larger values than the TE-TM splitting in 2D MCs.

The final term in Eq. (4) accounts for energy relaxation processes of condensed polaritons:

$$\Re[\psi(\vec{r},t)] = -\nu(\hat{E}_{\rm LP} - \mu(\vec{r},t))\psi(\vec{r},t), \tag{7}$$

where ν is a phenomenological parameter determining the strength of energy relaxation [19,26] and $\mu(\vec{r},t)$ is a local effective chemical potential that conserves the polariton population. These terms cause the relaxation of any kinetic energy of polaritons and allow the population of lower-energy states trapped between the pump-induced potentials.

For the simulation that produces the results in Figs. 8 and 9, the following parameters are used: $\alpha_1 = 2.4 \times 10^{-3}$ meV μm^2, $\hbar\nu = 0.14$, $\Gamma = 0.0366$ meV (Ref. [27]), $\alpha_2 = -0.2\alpha_1$ (Ref. [11]). The LP dispersion is characterized by an effective mass $m = 7.3 \times 10^{-5} m_e$, fitted to Fig. 1, where m_e is the free-electron mass. $G_+ = 1.0$ and $G_- = 0.7$ are fitted to the measured space- and polarization-resolved energy distributions. $W_0 = 0.185$ meV, $\rho = 0.5$, and $\Delta_{\rm TM,TE} = -0.15$ meV. The width of the condensation rate profile is taken to be $L = 10\ \mu$m. The calculations were performed using an adaptive step Adams-Bashforth-Moulton error-corrector procedure in a grid with 384×32 points. The polariton wave functions were initialized with a weak intensity noise, the distribution of which was found to have no effect on the end result. After a period of initial dynamics, energy distributions are obtained from Fourier transformation over a time window of 250 ps.

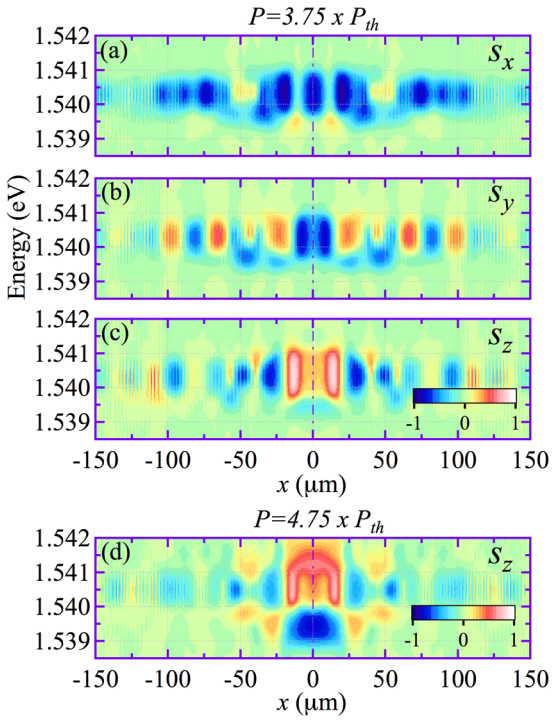

FIG. 9. (Color online) Simulation on the Stokes parameters of the polariton PL as a function of energy and spatial position (x): (a) s_x, (b) s_y, and (c) s_z, respectively, under nonresonant, circularly polarized excitation, with a pump power $P = 3.75 \times P_{\rm th}$. (d) s_z under a higher pump power excitation $4.75 \times P_{\rm th}$. The degree of polarization is coded in a linear, false color scale.

The simulated images shown in Figs. 8 and 9(a)–9(c) can be compared to the experimental results in Figs. 4(a-c) and 5(a-c), respectively. The calculated dependence of s_z on pump power can be observed in Figs. 9(c) and 9(d): a blueshift of the maximum polariton energy as well as a slight reduction of the spin precession with increasing power is obtained, in agreement with the experiments reported in Figs. 7(a-1) and 7(a-2). The localized, polarized, incoherent pumping generates two distributions of polaritons separated both in polarization and in energy at $x = 0$: while the majority of polaritons are σ^+-polarized, a significant number of polaritons also condense into a σ^--polarized state, which has lower energy due to the spin-dependent blueshifts in the system $V_\sigma(\vec{r},t)$. A very good agreement between the experimental and theoretical (x,y) maps is obtained.

The potential $V_\sigma(\vec{r})$, which is mostly induced by hot excitons with the same spatial distribution as the pump, represents a strongly repulsive potential in the system that accelerates polaritons outward. The simulated energy- and space-resolved map of the s_x Stokes parameter, shown in Fig. 9(a), is also in reasonable agreement with the experimental results depicted in Fig. 5(a). As the accelerated polaritons move outward, their spins precess, due to the polarization splitting, giving rise to oscillations in s_y and s_z [see Figs. 9(b) and 9(c)] as in the experiments [Figs. 5(b) and 5(c)]. Note that the theoretical model does not reproduce directly oscillations in the spatial distribution of s_x. Theoretically, any polarization splitting in the system can always be represented by an effective magnetic field about which the Stokes vector rotates. It is impossible to find an effective magnetic field that causes oscillations between both negative and positive values in all three components of the Stokes vector simultaneously (even if multiple forms of splitting are present, the total effective magnetic field cannot make an angle greater than 45° with the s_x, s_y, and s_z axes simultaneously). We thus conclude that the experimentally observed oscillation in s_x is not directly due to spin precession caused by the polarization splitting. Instead, we speculate that the oscillations in s_x are linked to the oscillations in the total PL intensity, which competes with a background of incoherent polaritons that are linearly polarized due to the TE-TM splitting. Where the condensate intensity is high, s_x is given by the mean-field theoretical value, while when the condensate intensity is low there may well be incoherent polaritons, not accounted for in the mean-field theory, that give a different polarization. Consequently, oscillations in intensity give the impression of oscillations in the linear polarization degree represented by s_x. The oscillations in intensity are due to the 2D nature of the propagation, where both theory and experiment show that polaritons tend to travel at an angle to the x axis, being guided by reflections from the ridge edges. The intensity viewed along the x axis is then greatest when polaritons propagating off-axis cross the x axis.

V. CONCLUSIONS

In summary, we have studied the optical spin Hall effect in a quasi-1D MC, where the lateral confinement yields a suitable scenario for the intrabranch polariton energy relaxation, enriching the phenomenology of the polariton spin patterns. Thanks to a spectroscopic analysis of the optical spin Hall effect, we have shown that a phase shift in the oscillations of the s_y and s_z Stokes parameters results from the different speeds of propagation of polaritons. These oscillations collapse either when linearly polarized excitation is used or when the pump power of the circularly polarized excitation exceeds a certain level. Our results are interpreted within the framework of a mean-field model for polariton dynamics, which includes incoherent gain from a polarized exciton reservoir, the energy shift due to the reservoir, TE-TM splitting, and energy relaxation. The demonstration of the inversion of the polariton spin as it propagates or relaxes in energy is an important ingredient for realizing polaritonic circuits based on the spin degree of freedom.

ACKNOWLEDGMENTS

C.A. acknowledges financial support from the Spanish FPU scholarship. P.S. acknowledges the Greek GSRT program "ARISTEIA" (1978) and EU ERC "Polaflow" for financial support. The work was partially supported by the Spanish MEC MAT2011-22997 and EU-FP7 ITN INDEX (289968) projects.

[1] A. I. Tartakovskii, V. D. Kulakovskii, D. N. Krizhanovskii, M. S. Skolnick, V. N. Astratov, A. Armitage, and J. S. Roberts, Phys. Rev. B **60**, R11293(R) (1999).

[2] M. D. Martín, G. Aichmayr, L. Viña, and R. André, Phys. Rev. Lett. **89**, 077402 (2002).

[3] Ł. Kłopotowski, M. D. Martín, A. Amo, L. Viña, I. A. Shelykh, M. M. Glazov, G. Malpuech, A. V. Kavokin, and R. André, Solid State Commun. **139**, 511 (2006).

[4] E. Kammann, T. C. H. Liew, H. Ohadi, P. Cilibrizzi, P. Tsotsis, Z. Hatzopoulos, P. G. Savvidis, A. V. Kavokin, and P. G. Lagoudakis, Phys. Rev. Lett. **109**, 036404 (2012).

[5] P. G. Lagoudakis, P. G. Savvidis, J. J. Baumberg, D. M. Whittaker, P. R. Eastham, M. S. Skolnick, and J. S. Roberts, Phys. Rev. B **65**, 161310 (2002).

[6] A. Amo, T. C. H. Liew, C. Adrados, R. Houdre, E. Giacobino, A. V. Kavokin, and A. Bramati, Nat. Photon. **4**, 361 (2010).

[7] C. Adrados, T. C. H. Liew, A. Amo, M. D. Martín, D. Sanvitto, C. Antón, E. Giacobino, A. Kavokin, A. Bramati, and L. Viña, Phys. Rev. Lett. **107**, 146402 (2011).

[8] M. Sich, F. Fras, J. K. Chana, M. S. Skolnick, D. N. Krizhanovskii, A. V. Gorbach, R. Hartley, D. V. Skryabin, S. S. Gavrilov, E. A. Cerda-Méndez, K. Biermann, R. Hey, and P. V. Santos, Phys. Rev. Lett. **112**, 046403 (2014).

[9] G. Grosso, S. Trebaol, M. Wouters, F. Morier-Genoud, M. T. Portella-Oberli, and B. Deveaud, Phys. Rev. B **90**, 045307 (2014).

[10] C. Leyder, T. C. H. Liew, A. V. Kavokin, I. A. Shelykh, M. Romanelli, J. P. Karr, E. Giacobino, and A. Bramati, Phys. Rev. Lett. **99**, 196402 (2007).

[11] T. K. Paraïso, M. Wouters, Y. Léger, F. Morier-Genoud, and B. Deveaud-Plédran, Nat. Mater. **9**, 655 (2010).

[12] R. Cerna, Y. Léger, T. K. Paraïso, M. Wouters, F. Morier-Genoud, M. T. Portella-Oberli, and B. Deveaud, Nat. Commun. **4**, 2008 (2013).

[13] I. A. Shelykh, T. C. H. Liew, and A. V. Kavokin, Phys. Rev. Lett. **100**, 116401 (2008).

[14] R. Johne, I. A. Shelykh, D. D. Solnyshkov, and G. Malpuech, Phys. Rev. B **81**, 125327 (2010).

[15] T. C. H. Liew, A. V. Kavokin, and I. A. Shelykh, Phys. Rev. Lett. **101**, 016402 (2008).

[16] I. A. Shelykh, G. Pavlovic, D. D. Solnyshkov, and G. Malpuech, Phys. Rev. Lett. **102**, 046407 (2009).

[17] T. Espinosa-Ortega and T. C. H. Liew, Phys. Rev. B **87**, 195305 (2013).

[18] E. Wertz, L. Ferrier, D. D. Solnyshkov, R. Johne, D. Sanvitto, A. Lemaitre, I. Sagnes, R. Grousson, A. V. Kavokin, P. Senellart, G. Malpuech, and J. Bloch, Nat. Phys. **6**, 860 (2010).

[19] E. Wertz, A. Amo, D. D. Solnyshkov, L. Ferrier, T. C. H. Liew, D. Sanvitto, P. Senellart, I. Sagnes, A. Lemaître, A. V. Kavokin, G. Malpuech, and J. Bloch, Phys. Rev. Lett. **109**, 216404 (2012).

[20] T. Gao, P. S. Eldridge, T. C. H. Liew, S. I. Tsintzos, G. Stavrinidis, G. Deligeorgis, Z. Hatzopoulos, and P. G. Savvidis, Phys. Rev. B **85**, 235102 (2012).

[21] C. Anton, T. C. H. Liew, G. Tosi, M. D. Martin, T. Gao, Z. Hatzopoulos, P. S. Eldridge, P. G. Savvidis, and L. Vina, Appl. Phys. Lett. **101**, 261116 (2012).

[22] H. S. Nguyen, D. Vishnevsky, C. Sturm, D. Tanese, D. Solnyshkov, E. Galopin, A. Lemaître, I. Sagnes, A. Amo, G. Malpuech, and J. Bloch, Phys. Rev. Lett. **110**, 236601 (2013).

[23] C. Antón, T. C. H. Liew, J. Cuadra, M. D. Martín, P. S. Eldridge, Z. Hatzopoulos, G. Stavrinidis, P. G. Savvidis, and L. Viña, Phys. Rev. B **88**, 245307 (2013).

[24] C. Sturm, D. Tanese, H. S. Nguyen, H. Flayac, E. Galopin, A. Lemaître, I. Sagnes, D. Solnyshkov, A. Amo, G. Malpuech, and J. Bloch, Nat. Commun. **5**, 3278 (2014).

[25] C. Antón, T. C. H. Liew, D. Sarkar, M. D. Martín, Z. Hatzopoulos, P. S. Eldridge, P. G. Savvidis, and L. Viña, Phys. Rev. B **89**, 235312 (2014).

[26] M. Wouters, New J. Phys. **14**, 075020 (2012).

[27] C. Antón, T. C. H. Liew, G. Tosi, M. D. Martín, T. Gao, Z. Hatzopoulos, P. S. Eldridge, P. G. Savvidis, and L. Viña, Phys. Rev. B **88**, 035313 (2013).

[28] G. Panzarini, L. C. Andreani, A. Armitage, D. Baxter, M. S. Skolnick, V. N. Astratov, J. S. Roberts, A. V. Kavokin, M. R. Vladimirova, and M. A. Kaliteevski, Phys. Rev. B **59**, 5082 (1999).

[29] C. Leyder, M. Romanelli, J. P. Karr, E. Giacobino, T. C. H. Liew, M. M. Glazov, A. V. Kavokin, G. Malpuech, and A. Bramati, Nat. Phys. **3**, 628 (2007).

[30] A. Kavokin, G. Malpuech, and M. Glazov, Phys. Rev. Lett. **95**, 136601 (2005).

[31] M. Dyakonov and V. Perel, Phys. Lett. A **35**, 459 (1971).

[32] J. Sinova, D. Culcer, Q. Niu, N. A. Sinitsyn, T. Jungwirth, and A. H. MacDonald, Phys. Rev. Lett. **92**, 126603 (2004).

[33] W. Langbein and J. M. Hvam, Phys. Rev. Lett. **88**, 047401 (2002).

[34] A. Amo, T. C. H. Liew, C. Adrados, E. Giacobino, A. V. Kavokin, and A. Bramati, Phys. Rev. B **80**, 165325 (2009).

[35] M. Maragkou, C. E. Richards, T. Ostatnický, A. J. D. Grundy, J. Zajac, M. Hugues, W. Langbein, and P. G. Lagoudakis, Opt. Lett. **36**, 1095 (2011).

[36] W. Langbein, I. Shelykh, D. Solnyshkov, G. Malpuech, Y. Rubo, and A. Kavokin, Phys. Rev. B **75**, 075323 (2007).

[37] F. Manni, K. G. Lagoudakis, T. K. Paraïso, R. Cerna, Y. Léger, T. C. H. Liew, I. A. Shelykh, A. V. Kavokin, F. Morier-Genoud, and B. Deveaud-Plédran, Phys. Rev. B **83**, 241307(R) (2011).

[38] F. Manni, Y. Léger, Y. G. Rubo, R. André, and B. Deveaud, Nat. Commun. **4**, 2590 (2013).

[39] V. G. Sala, D. D. Solnyshkov, I. Carusotto, T. Jacqmin, A. Lemaître, H. Terças, A. Nalitov, M. Abbarchi, E. Galopin, I. Sagnes, J. Bloch, G. Malpuech, and A. Amo, arXiv:1406.4816.

[40] T. C. H. Liew, A. V. Kavokin, and I. A. Shelykh, Phys. Rev. B **75**, 241301 (2007).

[41] R. Hivet, H. Flayac, D. D. Solnyshkov, D. Tanese, T. Boulier, D. Andreoli, E. Giacobino, J. Bloch, A. Bramati, G. Malpuech, and A. Amo, Nat. Phys. **8**, 724 (2012).

[42] H. Flayac, D. D. Solnyshkov, and G. Malpuech, Phys. Rev. B **83**, 193305 (2011).

[43] P. Cilibrizzi, H. Ohadi, T. Ostatnicky, A. Askitopoulos, W. Langbein, and P. Lagoudakis, Phys. Rev. Lett. **113**, 103901 (2014).

[44] O. A. Egorov and F. Lederer, Opt. Lett. **39**, 4029 (2014).

[45] A. Werner, O. A. Egorov, and F. Lederer, Phys. Rev. B **90**, 165308 (2014).

[46] O. A. Egorov, A. Werner, T. C. H. Liew, E. A. Ostrovskaya, and F. Lederer, Phys. Rev. B **89**, 235302 (2014).

[47] K. V. Kavokin, I. A. Shelykh, A. V. Kavokin, G. Malpuech, and P. Bigenwald, Phys. Rev. Lett. **92**, 017401 (2004).

[48] P. Tsotsis, P. S. Eldridge, T. Gao, S. I. Tsintzos, Z. Hatzopoulos, and P. G. Savvidis, New J. Phys. **14**, 023060 (2012).

[49] T. Lecomte, V. Ardizzone, M. Abbarchi, C. Diederichs, A. Miard, A. Lemaitre, I. Sagnes, P. Senellart, J. Bloch, C. Delalande, J. Tignon, and P. Roussignol, Phys. Rev. B **87**, 155302 (2013).

[50] W. Xie, H. Dong, S. Zhang, L. Sun, W. Zhou, Y. Ling, J. Lu, X. Shen, and Z. Chen, Phys. Rev. Lett. **108**, 166401 (2012).

[51] G. Christmann, G. Tosi, N. G. Berloff, P. Tsotsis, P. S. Eldridge, Z. Hatzopoulos, P. G. Savvidis, and J. J. Baumberg, Phys. Rev. B **85**, 235303 (2012).

[52] H. Ohadi, E. Kammann, T. C. H. Liew, K. G. Lagoudakis, A. V. Kavokin, and P. G. Lagoudakis, Phys. Rev. Lett. **109**, 016404 (2012).

[53] M. Wouters and I. Carusotto, Phys. Rev. Lett. **99**, 140402 (2007).

[54] J. Keeling and N. G. Berloff, Phys. Rev. Lett. **100**, 250401 (2008).

[55] G. Dasbach, C. Diederichs, J. Tignon, C. Ciuti, P. Roussignol, C. Delalande, M. Bayer, and A. Forchel, Phys. Rev. B **71**, 161308 (2005).